Research Article

A Novel Bacterial Foraging Optimization Based Multimodal Medical Image Fusion Approach

Gurusigaamani Ayyanar Muthulingam
Department of Computer Science and Engineering, Kalasalingam Academy of Research and Education, Tamilnadu, India

Velmurugan Subbiah Parvathy*
Department of Electronics and Communication Engineering, Kalasalingam Academy of Research and Education, Tamilnadu, India

* Corresponding author. E-mail: s.p.velmurugan@klu.ac.in DOI: 10.14416/j.asep.2023.03.004
Received: 22 November 2022; Revised: 20 December 2022; Accepted: 17 February 2023; Published online: 21 March 2023

Abstract
Multimodal medical image fusion (MIF) is the procedure of integrating different images in single into multiple imaging modalities for increasing the image quality by preserving a certain feature. Medical image combination covered a tremendous count of hot topic areas, involving pattern recognition, image processing, artificial intelligence (AI), computer vision (CV), and machine learning (ML). In addition, MIF was more commonly applied in clinical for physicians to understand the lesion by the combination of various modalities of medicinal image. This article introduces a novel bacterial foraging optimization-based multimodal medical image fusion approach (BFO-M3IFA). The presented BFO-M3IFA technique considered two distinct patterns of the images as the input of systems and the outcome will be the fused image. Primarily, the BFO-M3IFA technique exploits Weiner filtering (WF) technique as an image pre-processing step to get rid of the noise. Besides, discrete wavelet transform (DWT) was applied for decomposing the image into distinct subbands. Afterward, the estimated coefficients of modality 1 and comprehensive coefficients of modality 2 are integrated and vice versa. At last, a fusion rule is generated to fuse the details of two image modalities and the optimal fusion rule parameter is chosen with utilize of BFO algorithm. The experimental validation of the BFO-M3IFA system was tested and outcomes ensured the improved performance of the BFO-M3IFA system on existing models.

Keywords: Medical image fusion, Imaging modality, Bacterial foraging optimization, Discrete wavelet transform, Fusion rule generation

1 Introduction

Great developments in the healthcare sector have resulted in several imaging sensors that improvised clinical decision making. The diagnosis cases generally have a look at distinct depths and structures of the human body, generally unseen by just one modality [1], [2]. Therefore, data in several sensors are merged altogether for constructing new images which could intimate the specialist more via its complementary data. Image fusion becomes a highly promising research subject in the domain of image analysis and computer vision (CV) [3]. It addresses several applications, which include infrared, clinical diagnosis, and remote sensing. At the same time, the rising demand for image fusion in the present healthcare systems, for example, the image-guided procedures and percutaneous image-guided interventions were predominantly because of the progression in a diversity of acquisition technology [4], [5]. The primary goal is to afford an algorithm, which potentially complies with various diagnostic modalities to output

one representation that could support specialists (i.e. radiologists, interventionists oncologists,) in their decision-making and prognosis process [6]. In spite of the idea's simplicity, the fusion method has to face several difficulties related, not just to the theoretical context, but also to the medical image's nature, usually badly contrasted with ambiguous data [7].

Medical image fusion (MIF) is of two types' multimodal fusion and single-mode fusion. Owing to the limitations of data provided by single-mode fusion, several authors started to engage themselves in the research work of multimodal fusion [8], [9]. During the domain of medical images, imaging techniques like Single-Photon Emission Computed Tomography (SPECT), Positron Emission Tomography (PET), Computed Tomography (CT), and Magnetic Resonance Imaging (MRI) have presented doctors with information on the structural characteristics of human body, soft tissue, etc. [10], [11]. Various imaging techniques have diverse features, and distinct sensors acquire various image data of similar parts. The main objective of the fusion was to attain fusion quality, perceived experiences, and superior contrast [12]. The fusion outcome must address the following conditions one is the fused image must maintain the data of source images totally and the second condition is the fused image must not generate several synthetic data, like artifacts; and finally bad states must be ignored, namely misregistration and noise [13], [14]. With the arrival of DL boom, a MIF technique on the basis of DL originated in 2017. In recent times, U-Net network, convolutional neural network (CNN), GAN, recurrent neural network (RNN), and other DL approaches were extensively employed in medicinal image segmentation and registration, while just U-Net and CNN networks had been implemented in the MIF. CNN refers to a type of NN for image processing, that is made up of fully connected layer, convolutional layer, and pooling layer [15]. DL structure for MIF involves MatConvNet, Caffe, Tensorflow, and much more.

In spite of the ML and DL models that existed in the earlier studies, it is still needed to enhance the hate speech classification performance. Because of the continual deepening of the model, the number of parameters of DL models also increases quickly which results in model overfitting. At the same time, fusion rules have a significant impact on the fusion efficiency of the model. Since the trial and error method for fusion rule selection is a tedious and erroneous process, metaheuristic algorithms can be applied. Therefore, in this work, a metaheuristic algorithm is used for hyperparameter tuning.

Wang *et al.* [16] recommend a multimodal color MIF technique on the basis of geometric algebra DCT (GA-DCT). The GA-DCT method compiles the GA characters that indicate the multi-vector signal entirely, which could enhance the fusion image quality and ignore a large number of complicated functions based on decoding and encoding. Alseelawi *et al.* [17] suggested an effectual policy for multimodal MIF related to a hybrid technique of DTCWT and NSCT. In [18], a new MIF by utilizing side window filtering (SWF) and gradient domain guided filter random walk (GDGFRW) in the framelet transform (FT) field was provided. Initially, FT can be conducted on the original multi-modal source imageries for obtaining the residual representations and corresponding approximation. Next, a new method-GDGFRW that compiles the superiorities of random walks and gradient domain guided filtering was built for interpreting the estimated sub-bands, whereas the residual sub-bands were merged by SWF.

Shehanaz *et al.* [19] projected an optimum weighted average fusion (OWAF) for multi-modal MIF for improvising the multimodal mapped outcomes. In this technique, conventional DWT was utilized to decomposition of input multiples modality to several sub-groups. The resultant energy bands are weighted by making use of optimum weights, gained with the help of familiar PSO. In [20], siamese convolutional networks can be implemented for creating a weight map that combines the pixel movement data from more than two multimodalities of medicinal images. The MIF procedure was conducted in a multiscale manner through medical image pyramids that were highly dependable on human visual insight.

Azam *et al.* [21] present a novel Patch Adaptive Structure Decomposition employing the Multi-Exposure Fusion (MEF) approach for enhancing the local contrast of laparoscopic images for optimum visualization. The spatial linear saturation was executed for enhancing image contrast and for adjusting the image saturation. In [22], a Multi-resolution Rigid Registration (MRR) approach was utilized for multi-modal image registration but DWT together with Principal Component

Averaging (PCAv) was employed for image fusion. In [23], a new weighted parameter adaptive dual channel PCNN (WPADCPCNN) related medical fusion system was presented in non-sub sampled shearlet transform domain for fusing the MRI and SPECT images of AIDS dementia difficult and Alzheimer's disease patients.

Sengupta *et al.* [24] establish the 3 quantitative fusion metrics for assessing the quality of the image fusions technique. The presented metrics depend on edge data which is attained utilizing fractional order differentiation. Edge and orientation strengths can be provided as to 3 sigmoidal functions individually to estimate the values of 3 normalization weight metrics for fused images equivalent to source images. In [25], an image fusion system for CT and PET images dependent upon AWT and RF learning algorithms were presented. Image entropy integrates the helpful data of CT and PET images from the presented method. AWT takes benefits on mallat WT. RF studies several trees for obtaining superior forecast efficacy than any other constituent learning approach.

This article introduces a novel bacterial foraging optimization based multimodal medical image fusion approach (BFO-M3IFA). The presented BFO-M3IFA technique exploits Weiner filtering (WF) technique as an image pre-processing step to get rid of the noise. Besides, discrete wavelet transform (DWT) was executed for decomposing the image into distinct subbands. Afterward, the estimate coefficients of modality 1 and comprehensive coefficients of modality 2 were integrated and vice versa. Finally, a fusion rule is generated to fuse the details of two image modalities and the optimal fusion rule parameter is chosen with utilize of BFO algorithm. The experimental validation of the BFO-M3IFA system was tested using a set of medical images.

- An intelligent BFO-M3IFA technique comprising pre-processing, DWT based decomposition, and BFO based fusion rule generation is presented. To the best of our knowledge, the BFO-M3IFA model has never been presented in the literature.
- A novel BFO algorithm is employed for optimal fusion rule generation in the medical image fusion process, which helps to attain enhanced performance.
- Validate the performance of the BFO-M3IFA technique on medical CT and MRI images.

The rest of the paper is organized as follows. Section 2 introduces the methods, section 3 provides results and discussion and section 4 concludes the paper.

2 Methods

In this study, a novel BFO-M3IFA system was introduced to generate fusion of different medical imaging modalities. The presented BFO-M3IFA technique considered two distinct patterns of the images as the input of systems and the outcome will be fused images. Primarily, the presented BFO-M3IFA technique preprocessed the input images by the use of WF technique. Next, the DWT decomposition approach is used to decompose the image into distinct subbands. Afterward, the estimate coefficients of modality 1 and comprehensive coefficients of modality 2 were integrated and vice versa. Lastly, a fusion rule is generated to fuse the details of two image modalities and the optimal fusion rule parameter is chosen with utilize of BFO algorithm.

2.1 *Image pre-processing*

Primarily, the BFO-M3IFA technique exploits WF technique as an image pre-processing step to get rid of the noise. The wiener function executes a WF (a kind of linear filter) for image adaptably, tailoring itself to local image difference [26]. When the difference was huge, WF acts little smoothing. When it can be smaller, Wiener executes further smoothing. This technique frequently takes optimum outcomes than linear filters. The adaptive filtering was further selected than equivalent linear filtering, preserved edges, and other higher frequency part of images. Besides, there are no designed tasks; the wiener2 function manages every primary computation and executes the filter to input images. Wiener2, but does need further computation time than a linear filter.

The Fourier domain of WF is $G(u,v) = H \times (u,v)/[|H(\mathrm{u,v})|2\ Ps(u,v) + Pn(u,v)]$. Whereas $H \times (u,v)$ implies the complex conjugate of degradation function, $Pn(u,v)$ denotes the power spectral density of noises, $Ps(u,v)$ signifies the power spectral density of non-degraded images $H(u,v)$ represents the degradation function.

2.2 *Image decomposition*

At this stage, the DWT is applied to decompose the image into distinct subbands. Following the process of enhancement, the input image is decomposed through DWT. The 2D-DWT generates the four subbands, such as LL HH, LH, and HL images [27]. At this point, the HH images have the diagonal detail coefficients HL images comprise the vertical detail coefficient, LL images include an approximate coefficient, and LH images involve the horizontal detail coefficient. As a result, the LL image is regarded as approximate coefficients, and LL, LH, and HL images are assumed to be co-efficient. The wavelet decomposition outcome of I_1 is shown below. The detailed and approximation coefficient of I_1 are calculated using the below Equations (1)–(4),

$$I_{\Phi}^{1}(v_0,i,j)=\frac{1}{\sqrt{IJ}}\sum_{x=0}^{I-1}\sum_{y=0}^{J-1} I(x,y)\Phi(v_0,x,y) \quad (1)$$

$$I_{\Psi}^{1H}(v_0,i,j)=\frac{1}{\sqrt{IJ}}\sum_{x=0}^{I-1}\sum_{y=0}^{J-1} I(x,y)\ \Psi^{H}(v_0,x,y) \quad (2)$$

$$I_{\Psi}^{1V}(v_0,i,j)=\frac{1}{\sqrt{IJ}}\sum_{x=0}^{I-1}\sum_{y=0}^{J-1} I(x,y)\ \Psi^{V}(v_0,x,y) \quad (3)$$

$$I_{\Psi}^{1D}(v_0,i,j)=\frac{1}{\sqrt{IJ}}\sum_{x=0}^{I-1}\sum_{y=0}^{J-1} I(x,y)\ \Psi^{H}(v_0,x,y) \quad (4)$$

The wavelet decomposition output of I_2 images is shown below. The detailed and approximation coefficient of I_2 are calculated using the below Equations (5)–(8),

$$I_{\Phi}^{2}(v_0,i,j)=\frac{1}{\sqrt{IJ}}\sum_{x=0}^{I-1}\sum_{y=0}^{J-1} I(x,y)\Phi(v_0,x,y) \quad (5)$$

$$I_{\Psi}^{2H}(v_0,i,j)=\frac{1}{\sqrt{IJ}}\sum_{x=0}^{I-1}\sum_{y=0}^{J-1} I(x,y)\ \Psi_{(v,x,y)}^{H} \quad (6)$$

$$I_{\Psi}^{2V}(v_0,i,j)=\frac{1}{\sqrt{IJ}}\sum_{x=0}^{I-1}\sum_{y=0}^{J-1} I(x,y)\ \Psi_{(v,x,y)}^{V} \quad (7)$$

$$I_{\Psi}^{2D}(v_0,i,j)=\frac{1}{\sqrt{IJ}}\sum_{x=0}^{I-1}\sum_{y=0}^{J-1} I(x,y)\ \Psi_{(v,x,y)}^{D} \quad (8)$$

2.3 *Primary fusion*

Afterward the image decomposition, the CT and MRI images are merged. At this point, detail coefficients of I_2 (CT) and approximate coefficient of input image I_1 (MRI) are integrated for obtaining merged images F_1^{fusion} using the below Equation (9),

$$F_1^{fusion}=I_{\Phi}^{1}(v_0,i,j)+I_{\Psi_{(v,i,j)}}^{2i} \quad (9)$$

When $i = \{H, V, D\}$, gives horizontal, vertical, and diagonal particulars of input. In the same way, approximation coefficient of I_2 (CT) and detailed coefficient of input image I_1 (MRI) are integrated for attaining F_2^{fusion} using the below Equation (10),

$$F_2^{fusion}=I_{\Phi}^{2}(v_0,i,j)+I_{\Psi_{(v,i,j)}}^{1i} \quad (10)$$

2.4 *Final fusion*

At last, a fusion rule is generated to fuse the details of two image modalities and the optimal fusion rule parameter is chosen by the use of BFO algorithm. In the last phase, F_1^{fusion} and F_2^{fusion} images are combined by utilizing fusion rule that is shown in the following.

$$F^{Fusion}=W_1\times F_1^{fusion}+W_2\times F_2^{fusion} \quad (11)$$

Equation (11), W_1 and W_2 indicates the weight value. To improve the fusion quantity, the weight value is chosen in an optimum way.

The initiation of the conventional BFO approach comprises two major contents: bacterial and solution space initiation [28]. The position of *i-th* bacterium in the optimization is represented as b $P_i(j,k,l)$, was corresponding to the optimal parameter of solutions, that is $P_i(j,k,l) = [m_1, m_2,\ldots, m_D]$. Figure 1 depicts the steps involved in BFO technique.

As a result, the fitness of *i-th* bacterium in the optimization is characterized as $J_i(j,k,l)$, is determined by the function of bacterium position:

$$J_i(j,k,l) = f(P_i(j,k,l)) = f_{i,j,k,l}(m_1,m_2,\ldots,\ m_D). \quad (12)$$

From Equation (12), the lower value of function indicates higher fitness. *i* signifies *i-th* bacterium, whereby *j*, *k*, and *l* are related to the centralized process of the BFO technique: reproduction, dispersal,

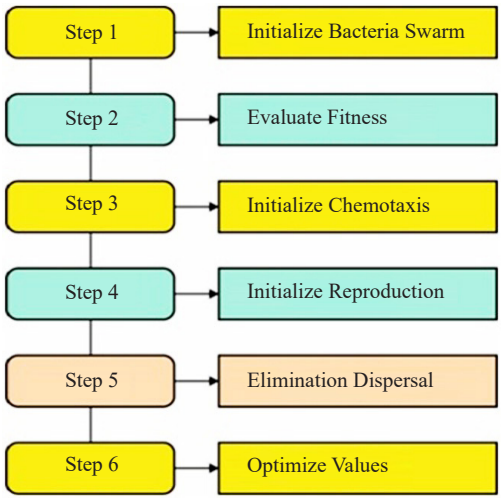

Figure 1: Steps involved in BFO.

elimination, and chemotaxis.

2.4.1 Chemotaxis

In this phase, flipping movement and massive quantity of swimming are considered. In *j-th* chemotaxis process, the motion of *i-th* bacterium is demonstrated in the below Equation (13) as follows:

$$P_i(j+1,k,l) = P_i(j,k,l) + \frac{\Delta(i)}{\sqrt{\Delta^T(i)\Delta(i)}} C(i)n, \qquad (13)$$

Each component of (i) is arithmetical value that lies within [–1,1], whereby the initiation is set to arbitrary number. When the *i-th* bacterium identifies a higher fitness position as a promising atmosphere in *j-th* chemotaxis, it undergoes moves in a comparable direction dependent on the time. Instead (i) chooses an arbitrary direction.

2.4.2 Swarming

The bacteria are assumed that repulsion and attractive. The numerical relationship is defined as follows:

$$J_{cc}(P_i) = \sum_{i=1}^{s}\left[-d_{att}\ \exp\left(-\omega_{att}\sum_{m=1}^{p}\left(P_{i,m}-\overline{P_m}\right)^2\right)\right] + \sum_{i=1}^{s}\left[h_{rep}\ \exp\left(-\omega_{rep}\sum_{m=1}^{p}\left(P_{i.m}-\overline{P_m}\right)\right)\right], \qquad (14)$$

In Equation (14), d_{att} indicates depth at the attraction material was released using *i-th* bacterium, while ω_{att} denotes the width of attracted material. Likewise, 2 bacteria could not be in precisely the comparable site, the repulsion is adopted as h_{repand} ω_{rep}. Later, in the swarming process, the fitness of *i-th* bacterium was shown in Equation (15) as follows:

$$J_i(j+1,k,l) = J_i(j,k,l) + J_{cc}(P_i(j,k,l)) \qquad (15)$$

2.4.3 Reproduction

The bacteria replicate when they accomplish the finest atmosphere; if not, they die. As a result, of the chemotaxis and swarming process, the fitness of whole bacteria is calculated using the Equation (16):

$$J_{i,health} = \sum_{j=1}^{Nc} J_i(j,k,l). \qquad (16)$$

Half of bacteria in state $S_r = \left(\frac{S}{2}\right)$ are preferred to survive, where remaining will die.

2.4.4 Elimination and dispersal

Later reproduction, bacterium was distributed by possibility of P_{ed}, but the total amount of bacteria remains comparable. Once a bacterium was detached, it can be distributed arbitrarily to a novel site.

$r = random$ [0,1];

$$P_i(j,k,l) = \begin{cases} P_i(j,k,l) & r > P_{ed}, \\ m_1', m_2', \ldots m_p' & r < P_{ed}. \end{cases} \qquad (17)$$

As shown in Equation (17), removal performs when $r_i < P_{ed}$.The unique position of *i-th* bacterium P_i was substituted with $P_i' = (m_1', m_2', \ldots, m_D'$ Accordingly, an m variable is upgraded to m' parameter.

3 Results and Discussion

The proposed multi-focus image fusion is implemented in the platform MATLAB R2015a. This section inspects the experimental validation of the BFO-M3IFA model using a medical image dataset from (http://www.med.harvard.edu/aanlib/). The dataset holds medical CT and MRI images. Some sample images are depicted

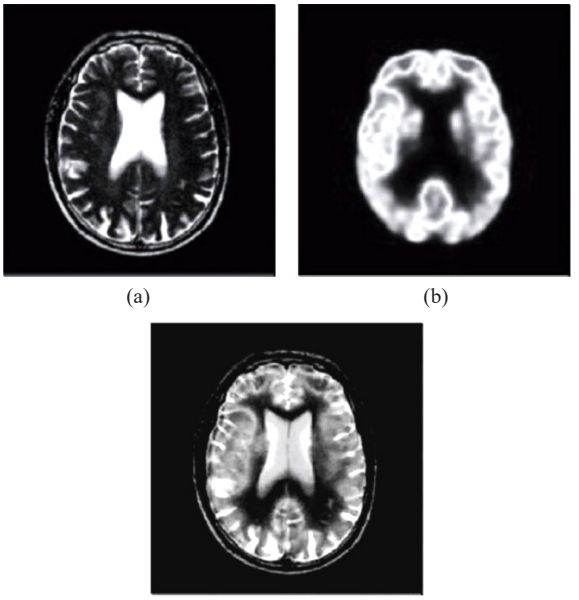

(a) (b) (c)

Figure 2: Sample images (a) MRI Image (b) CT Image (c) Fused Image.

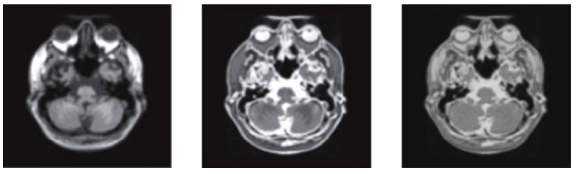

(a) MRI (b) CT (c) Fused image

Figure 3: Sample fused output.

in Figure 2. Each input image in the dataset has the same size 512 × 512 with 256 grayscale levels. Figure 3 depicts a visualization of sample fusion output.

Table 1 and Figure 4 offer a comprehensive entropy examination of the BFO-M3IFA system with other approaches under distinct sample images [29]. The experimental values exposed that the BFO-M3IFA approach has accomplished enhanced performance with superior values of entropy. For sample, with sample 1, the BFO-M3IFA method has offered higher entropy of 7.0819, whereas the DWT-BCSA, DWT-CSA, and DWT-GA techniques have obtained lower entropy of 6.7649, 6.3379, and 6.1068 respectively. Followed by, for sample 3, the BFO-M3IFA method has rendered higher entropy of 6.5919 whereas the DWT-BCSA, DWT-CSA, and DWT-GA approaches have gained lower entropy of 6.2489, 5.6469, and

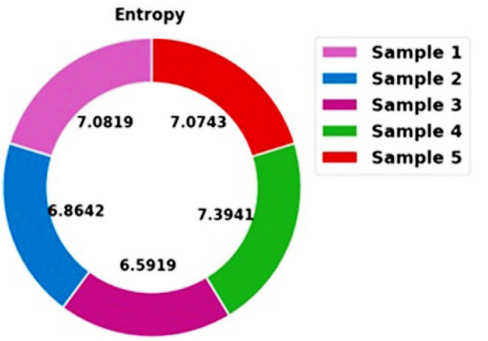

Figure 4: Entropy analysis of BFO-M3IFA approach with distinct sample images.

5.1188 correspondingly. In addition, with sample 5, the BFO-M3IFA algorithm has provided higher entropy of 7.0743 whereas the DWT-BCSA, DWT-CSA, and DWT-GA methods have reached lower entropy of 6.7513, 6.2219, and 5.6028, correspondingly.

Table 1: Entropy analysis of BFO-M3IFA approach with existing methods distinct sample images

Entropy(bits/pixel)				
No. of Sample Images	**BFO-M3IFA**	**DWT-BCSA**	**DWT-CSA**	**DWT-GA**
Sample 1	7.0819	6.7649	6.3379	6.1068
Sample 2	6.8642	6.4812	6.1199	5.6547
Sample 3	6.5919	6.2489	5.6469	5.1188
Sample 4	7.3941	7.0631	6.3405	5.8113
Sample 5	7.0743	6.7513	6.2219	5.6028

Table 2 and Figure 5 present a detailed SSIM investigation of the BFO-M3IFA method with other techniques under distinct sample images. The experimental values inferred that the BFO-M3IFA approach has established improvised performance with higher values of SSIM. For sample, for sample 1, the BFO-M3IFA method has rendered a higher SSIM of 92.38%, whereas the DWT-BCSA, DWT-CSA, and DWT-GA methodologies have acquired lower SSIM of 90.37, 85.50, and 81.18% correspondingly. Subsequently, with sample 3, the BFO-M3IFA method has offered higher SSIM of 81.63%, whereas the DWT-BCSA, DWT-CSA, and DWT-GA approaches have obtained lower SSIM of 79.58, 75.62, and 71.66% correspondingly. Moreover, with sample 5, the BFO-M3IFA model has presented higher SSIM of

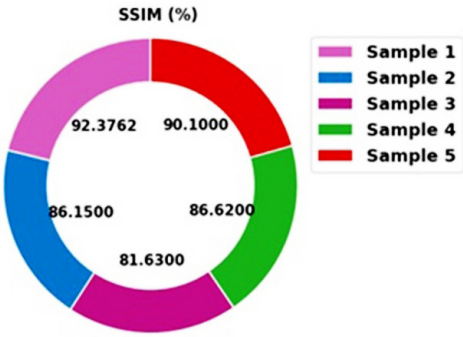

Figure 5: SSIM analysis of BFO-M3IFA approach with distinct sample images.

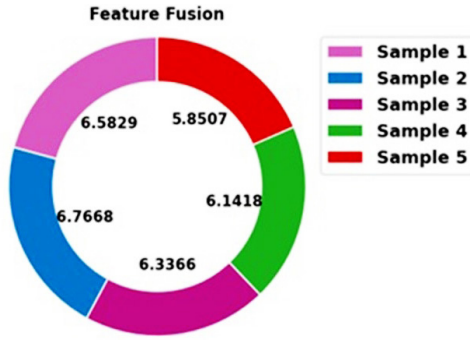

Figure 6: Feature fusion analysis of BFO-M3IFA approach with distinct sample images.

90.10% whereas the DWT-BCSA, DWT-CSA, and DWT-GA techniques have attained lower SSIM of 87.58, 80.40, and 75.05% correspondingly.

Table 2: SSIM analysis of BFO-M3IFA approach with existing methods distinct sample images

SSIM (%)				
No. of Sample Images	**BFO-M3IFA**	**DWT-BCSA**	**DWT-CSA**	**DWT-GA**
Sample 1	92.38	90.37	85.50	81.18
Sample 2	86.15	83.69	79.28	75.36
Sample 3	81.63	79.58	75.62	71.66
Sample 4	86.62	83.74	78.32	73.53
Sample 5	90.10	87.58	80.40	75.05

Table 3 and Figure 6 offer a detailed fusion investigation of the BFO-M3IFA methodology with other models under distinct sample images. The experimental values represented by the BFO-M3IFA approach have accomplished improvised performance with increased values of feature fusion. For instance, with sample 1, the BFO-M3IFA method has provided higher feature fusion of 6.5829, whereas the DWT-BCSA, DWT-CSA, and DWT-GA methods have gained lower feature fusion of 6.3009, 5.3557, and 4.3142 correspondingly. Next, with sample 3, the BFO-M3IFA technique has rendered higher feature fusion of 6.3366, whereas the DWT-BCSA, DWT-CSA, and DWT-GA approaches have reached lower feature fusion of 6.0046, 4.4798, and 4.3017, respectively. Moreover, with sample 5, the BFO-M3IFA method has presented higher feature fusion of 5.8507, whereas the DWT-BCSA, DWT-CSA, and DWT-GA models have obtained lower feature fusion of 5.4897, 5.3857, and 4.1706, correspondingly.

Table 3: Feature fusion analysis of BFO-M3IFA approach with existing methods distinct sample images

Feature Fusion				
No. of Sample Images	**BFO-M3IFA**	**DWT-BCSA**	**DWT-CSA**	**DWT-GA**
Sample 1	6.5829	6.3009	5.3557	4.3142
Sample 2	6.7668	6.4068	5.9320	4.7871
Sample 3	6.3366	6.0046	4.4798	4.3017
Sample 4	6.1418	5.8748	5.3253	5.2419
Sample 5	5.8507	5.4897	5.3857	4.1706

From the detailed results and discussion, it is assumed that the BFO-M3IFA model has shown enhanced performance over all the other models.

4 Conclusions

In this study, a novel BFO-M3IFA system was introduced for generating fusion of different medical imaging modalities. The presented BFO-M3IFA technique considered two distinct patterns of the images as the input of systems and the outcome will be the fused image. The BFO-M3IFA technique encompasses a series of processes namely WF preprocessing, DWT decomposition, coefficient estimation, fusion rule generation, and BFO based fusion rule optimization. The experimental validation of the BFO-M3IFA system was tested utilizing a set of medical images and the outcomes ensured the improved performance of the BFO-M3IFA system on

existing models. In future, the presented model can be extended to the design of deep learning based medical image classification tools. In future, multiple other medical modalities can be included in fusion process.

Author Contributions

G.A.M. Conceptualization, original draft, Methodology, Formal analysis, Resources, Validation, Software; V.S.P. Writing – review & editing, Project administration, Resources, Validation. All authors have read and agreed to the published version of the manuscript.

Conflict of Interest

The authors declare no conflict of interest.

References

[1] B. Huang, F. Yang, M. Yin, X. Mo, and C. Zhong, "A review of multimodal medical image fusion techniques," *Computational and Mathematical Methods in Medicine*, vol. 2020, pp. 1–16, Apr. 2020, doi:10.1155/2020/8279342.

[2] B. Rajalingam and R. Priya, "Multimodality medical image fusion based on hybrid fusion techniques," *International Journal of Engineering and Manufacturing Science*, vol. 7, no. 1, pp. 22–29, Nov. 2017.

[3] T. Tirupal, B. C. Mohan, and S. S. Kumar, "Multimodal medical image fusion techniques–A review," *Current Signal Transduction Therapy*, vol. 16, no. 2, pp. 142–163, Feb. 2020, doi: 10.2174/1574362415666200226103116.

[4] M. A. Azam, K. B. Khan, S. Salahuddin, E. Rehman, S. A. Khan, M. A. Khan, S. Kadry, and A. H. Gandomi, "A review on multimodal medical image fusion: Compendious analysis of medical modalities, multimodal databases, fusion techniques and quality metrics," *Computers in Biology and Medicine*, vol. 144, May 2022, Art. no. 105253, doi: 10.1016/j.compbiomed.2022.105253.

[5] Y. Li, J. Zhao, Z. Lv, and J. Li, "Medical image fusion method by deep learning," *International Journal of Cognitive Computing in Engineering*, vol. 2, pp. 21–29, Jun. 2021, doi:10.1016/j.ijcce.2020.12.004.

[6] W. Tan, P. Tiwari, H. M. Pandey, C. Moreira, and A. K. Jaiswal, "Multimodal medical image fusion algorithm in the era of big data," *Neural Computing and Applications*, pp. 1–21, Jul. 2020, doi: 10.1007/s00521-020-05173-2.

[7] S. P. Yadav and S. Yadav, "Image fusion using hybrid methods in multimodality medical images," *Medical & Biological Engineering & Computing*, vol. 58, pp. 669–687, Jan. 2020, doi: 10.1007/s11517-020-02136-6.

[8] B. Rajalingam and R. Priya, "Multimodal medical image fusion using various hybrid fusion techniques for clinical treatment analysis," *Smart Construction Research*, vol. 2, no. 4, 2018, doi: 10.18686/scr.v2i4.594.

[9] K. B. Khan, A. A. Khaliq, M. Shahid, and H. Ullah, "Poisson noise reduction in scintigraphic images using gradient adaptive trimmed meanfilter," in *2016 International Conference on Intelligent Systems Engineering (ICISE)*, 2016, pp. 301–305, doi: 10.1109/INTELSE.2016.7475138.

[10] K. B. Khan, M. Shahid, H. Ullah, E. Rehman, and M. M. Khan, "Adaptive trimmed mean autoregressive model for reduction of Poisson noise in scintigraphic images," *IIUM Engineering Journal*, vol. 19, no. 2, pp. 68–79, 2018.

[11] K. B. Khan, A. A. Khaliq, M. Shahid, and J. A. Shah, "A new approach of weighted gradient filter for denoising of medical images in the presence of Poisson noise," *Tehnicki Vjesnik - Technical Gazette*, vol. 23, no. 6, pp. 1755–1762, 2016.

[12] M. A. Azam, K. B. Khan, S. Salahuddin, E. Rehman, S. A. Khan, M. A. Khan, S. Kadry, A. H. Gandomi, "A review on multimodal medical image fusion: Compendious analysis of medical modalities, multimodal databases, fusion techniques and quality metrics," *Computers in Biology and Medicine*, vol. 144, Art. no. 105253, 2022.

[13] Z. Zhu, X. He, G. Qi, Y. Li, B. Cong, and Y. Liu, "Brain tumor segmentation based on the fusion of deep semantics and edge information in multimodal MRI," *Information Fusion*, vol. 91, pp. 376–387, 2023.

[14] S. Goyal, V. Singh, A. Rani, and N. Yadav, "Multimodal image fusion and denoising in NSCT domain using CNN and FOTGV," *Biomedical Signal Processing and Control*,

vol. 71, Jan. 2022, Art. no. 103214, doi: 10.1016/j.bspc.2021.103214.

[15] H. Hermessi, O. Mourali, and E. Zagrouba, "Multimodal medical image fusion review: Theoretical background and recent advances," *Signal Processing*, vol. 183, Jun. 2021, Art. no. 108036, doi: 10.1016/j.sigpro.2021.108036.

[16] R. Wang, N. Fang, Y. He, Y. Li, W. Cao, and H. Wang, "Multi-modal medical image fusion based on geometric algebra discrete cosine transform," *Advances in Applied Clifford Algebras*, vol. 32, no. 2, pp. 1–23, Feb. 2022, doi: 10.1007/s00006-021-01197-6.

[17] N. Alseelawi, H. T. Hazim, and H. T. S. Alrikabi, "A novel method of multimodal medical image fusion based on hybrid approach of NSCT and DTCWT," *International Journal of Online & Biomedical Engineering*, vol. 18, no. 03, Mar. 2022, doi: 10.3991/ijoe.v18i03.28011.

[18] W. Kong, Q. Miao, R. Liu, Y. Lei, J. Cui, and Q. Xie, "Multimodal medical image fusion using gradient domain guided filter random walk and side window filtering in framelet domain," *Information Sciences*, vol. 585, pp. 418–440, 2022.

[19] S. Shehanaz, E. Daniel, S. R. Guntur, and S. Satrasupalli, "Optimum weighted multimodal medical image fusion using particle swarm optimization," *Optik*, vol. 231, Art. no. 166413, Apr. 2021, doi: 10.1016/j.ijleo.2021.166413.

[20] B. Rajalingam and R. Priya, "Multimodal medical image fusion based on deep learning neural network for clinical treatment analysis," *International Journal of ChemTech Research*, vol. 11, no. 6, pp. 160–176, May 2018.

[21] M. A. Azam, K. B. Khan, E. Rehman, and S. U. Khan, "Smoke removal and image enhancement of laparoscopic images by an artificial multi-exposure image fusion method," *Soft Computing*, vol. 26, pp. 8003–8015, 2022.

[22] M. A. Azam, K. B. Khan, M. Ahmad, and M. Mazzara, "Multimodal medical image registration and fusion for quality Enhancement," *Computers, Materials & Continua*, vol. 68, no. 1, pp. 821–840, 2021 .

[23] C. Panigrahy, A. Seal, and N. K. Mahato, "MRI and SPECT image fusion using a weighted parameter adaptive dual channel PCNN," *IEEE Signal Processing Letters*, vol. 27, pp. 690–694, 2020.

[24] A. Sengupta, A. Seal, C. Panigrahy, O. Krejcar, and A. Yazidi, "Edge information based image fusion metrics using fractional order differentiation and sigmoidal functions," *IEEE Access*, vol. 8, pp. 88385–88398, 2020.

[25] A. Seal, D. Bhattacharjee, M. Nasipuri, D. Rodríguez - Esparragón, E. Menasalvas, and C. Gonzalo-Martin, "PET-CT image fusion using random forest and à-trous wavelet transform," *International Journal for Numerical Methods in Biomedical Engineering*, vol. 34, no. 3, Art. no. e2933, 2018, doi: 10.1002/cnm.2933.

[26] C. V. Cannistraci, F. M. Montevecchi, and M. Alessio, "Median-modified Wiener filter provides efficient denoising, preserving spot edge and morphology in 2-DE image processing," *Proteomics*, vol. 9, no. 21, pp. 4908–4919, Nov. 2009, doi: 10.1002/pmic.200800538.

[27] S. Lahmiri and M. Boukadoum, "Hybrid discrete wavelet transform and gabor filter banks processing for features extraction from biomedical images," *Journal of Medical Engineering*, vol. 2013, Apr. 2013, doi: 10.1155/2013/104684.

[28] Z. Li, Y. Qian, H. Wang, X. Zhou, G. Sheng, and X. Jiang, "Partial discharge fault diagnosis based on zernike moment and improved bacterial foraging optimization algorithm," *Electric Power Systems Research*, vol. 207, Jun. 2022, Art. no. 107854, doi: 10.1016/j.epsr.2022.107854.

[29] V. S. Parvathy and S. Pothiraj, "Multi-modality medical image fusion using hybridization of binary crow search optimization," *Health Care Management Science*, vol. 23, no. 4, pp. 661–669, 2020, doi: 10.1007/s10729-019-09492-2.